First search for dark-trident processes using the MicroBooNE detector

P. Abratenko,[38] O. Alterkait,[38] D. Andrade Aldana,[15] L. Arellano,[21] J. Asaadi,[37] A. Ashkenazi,[35]
S. Balasubramanian,[12] B. Baller,[12] G. Barr,[28] D. Barrow,[28] J. Barrow,[22, 25, 35] V. Basque,[12]
O. Benevides Rodrigues,[15] S. Berkman,[12, 24] A. Bhanderi,[21] A. Bhat,[7] M. Bhattacharya,[12] M. Bishai,[3] A. Blake,[18]
B. Bogart,[23] T. Bolton,[17] J. Y. Book,[14] M. B. Brunetti,[41] L. Camilleri,[10] Y. Cao,[21] D. Caratelli,[4] F. Cavanna,[12]
G. Cerati,[12] A. Chappell,[41] Y. Chen,[31] J. M. Conrad,[22] M. Convery,[31] L. Cooper-Troendle,[29] J. I. Crespo-Anadón,[6]
R. Cross,[41] M. Del Tutto,[12] S. R. Dennis,[5] P. Detje,[5] A. Devitt,[18] R. Diurba,[2] Z. Djurcic,[1] R. Dorrill,[15]
K. Duffy,[28] S. Dytman,[29] B. Eberly,[33] P. Englezos,[30] A. Ereditato,[7, 12] J. J. Evans,[21] R. Fine,[19] O. G. Finnerud,[21]
W. Foreman,[15] B. T. Fleming,[7] D. Franco,[7] A. P. Furmanski,[25] F. Gao,[4] D. Garcia-Gamez,[13] S. Gardiner,[12]
G. Ge,[10] S. Gollapinni,[19] E. Gramellini,[21] P. Green,[28] H. Greenlee,[12] L. Gu,[18] W. Gu,[3] R. Guenette,[21]
P. Guzowski,[21] L. Hagaman,[7] O. Hen,[22] C. Hilgenberg,[25] G. A. Horton-Smith,[17] Z. Imani,[38] B. Irwin,[25]
M. S. Ismail,[29] C. James,[12] X. Ji,[26] J. H. Jo,[3] R. A. Johnson,[8] Y.-J. Jwa,[10] D. Kalra,[10] N. Kamp,[22] G. Karagiorgi,[10]
W. Ketchum,[12] M. Kirby,[3, 12] T. Kobilarcik,[12] I. Kreslo,[2] M. B. Leibovitch,[4] I. Lepetic,[30] J.-Y. Li,[11] K. Li,[42] Y. Li,[3]
K. Lin,[30] B. R. Littlejohn,[15] H. Liu,[3] W. C. Louis,[19] X. Luo,[4] C. Mariani,[40] D. Marsden,[21] J. Marshall,[41]
N. Martinez,[17] D. A. Martinez Caicedo,[32] S. Martynenko,[3] A. Mastbaum,[30] I. Mawby,[41] N. McConkey,[39]
V. Meddage,[17] J. Micallef,[22, 38] K. Miller,[7] A. Mogan,[9] T. Mohayai,[12, 16] M. Mooney,[9] A. F. Moor,[5] C. D. Moore,[12]
L. Mora Lepin,[21] M. M. Moudgalya,[21] S. Mulleriababu,[2] D. Naples,[29] A. Navrer-Agasson,[21] N. Nayak,[3]
M. Nebot-Guinot,[11] J. Nowak,[18] N. Oza,[10] O. Palamara,[12] N. Pallat,[25] V. Paolone,[29] A. Papadopoulou,[1]
V. Papavassiliou,[27] H. B. Parkinson,[11] S. F. Pate,[27] N. Patel,[18] Z. Pavlovic,[12] E. Piasetzky,[35] I. Pophale,[18]
X. Qian,[3] J. L. Raaf,[12] V. Radeka,[3] A. Rafique,[1] M. Reggiani-Guzzo,[11, 21] L. Ren,[27] L. Rochester,[31] J. Rodriguez
Rondon,[32] M. Rosenberg,[38] M. Ross-Lonergan,[19] C. Rudolf von Rohr,[2] I. Safa,[10] G. Scanavini,[42] D. W. Schmitz,[7]
A. Schukraft,[12] W. Seligman,[10] M. H. Shaevitz,[10] R. Sharankova,[12] J. Shi,[5] E. L. Snider,[12] M. Soderberg,[34]
S. Söldner-Rembold,[21] J. Spitz,[23] M. Stancari,[12] J. St. John,[12] T. Strauss,[12] A. M. Szelc,[11] W. Tang,[36] N. Taniuchi,[5]
K. Terao,[31] C. Thorpe,[21] D. Torbunov,[3] D. Totani,[4] M. Toups,[12] Y.-T. Tsai,[31] J. Tyler,[17] M. A. Uchida,[5]
T. Usher,[31] B. Viren,[3] M. Weber,[2] H. Wei,[20] A. J. White,[7] S. Wolbers,[12] T. Wongjirad,[38] M. Wospakrik,[12]
K. Wresilo,[5] W. Wu,[29] E. Yandel,[4] T. Yang,[12] L. E. Yates,[12] H. W. Yu,[3] G. P. Zeller,[12] J. Zennamo,[12] and C. Zhang[3]

(The MicroBooNE Collaboration)[∗]

[1]*Argonne National Laboratory (ANL), Lemont, IL, 60439, USA*
[2]*Universität Bern, Bern CH-3012, Switzerland*
[3]*Brookhaven National Laboratory (BNL), Upton, NY, 11973, USA*
[4]*University of California, Santa Barbara, CA, 93106, USA*
[5]*University of Cambridge, Cambridge CB3 0HE, United Kingdom*
[6]*Centro de Investigaciones Energéticas, Medioambientales y Tecnológicas (CIEMAT), Madrid E-28040, Spain*
[7]*University of Chicago, Chicago, IL, 60637, USA*
[8]*University of Cincinnati, Cincinnati, OH, 45221, USA*
[9]*Colorado State University, Fort Collins, CO, 80523, USA*
[10]*Columbia University, New York, NY, 10027, USA*
[11]*University of Edinburgh, Edinburgh EH9 3FD, United Kingdom*
[12]*Fermi National Accelerator Laboratory (FNAL), Batavia, IL 60510, USA*
[13]*Universidad de Granada, Granada E-18071, Spain*
[14]*Harvard University, Cambridge, MA 02138, USA*
[15]*Illinois Institute of Technology (IIT), Chicago, IL 60616, USA*
[16]*Indiana University, Bloomington, IN 47405, USA*
[17]*Kansas State University (KSU), Manhattan, KS, 66506, USA*
[18]*Lancaster University, Lancaster LA1 4YW, United Kingdom*
[19]*Los Alamos National Laboratory (LANL), Los Alamos, NM, 87545, USA*
[20]*Louisiana State University, Baton Rouge, LA, 70803, USA*
[21]*The University of Manchester, Manchester M13 9PL, United Kingdom*
[22]*Massachusetts Institute of Technology (MIT), Cambridge, MA, 02139, USA*
[23]*University of Michigan, Ann Arbor, MI, 48109, USA*
[24]*Michigan State University, East Lansing, MI 48824, USA*
[25]*University of Minnesota, Minneapolis, MN, 55455, USA*
[26]*Nankai University, Nankai District, Tianjin 300071, China*
[27]*New Mexico State University (NMSU), Las Cruces, NM, 88003, USA*
[28]*University of Oxford, Oxford OX1 3RH, United Kingdom*
[29]*University of Pittsburgh, Pittsburgh, PA, 15260, USA*

^{30} Rutgers University, Piscataway, NJ, 08854, USA
^{31} SLAC National Accelerator Laboratory, Menlo Park, CA, 94025, USA
^{32} South Dakota School of Mines and Technology (SDSMT), Rapid City, SD, 57701, USA
^{33} University of Southern Maine, Portland, ME, 04104, USA
^{34} Syracuse University, Syracuse, NY, 13244, USA
^{35} Tel Aviv University, Tel Aviv, Israel, 69978
^{36} University of Tennessee, Knoxville, TN, 37996, USA
^{37} University of Texas, Arlington, TX, 76019, USA
^{38} Tufts University, Medford, MA, 02155, USA
^{39} University College London, London WC1E 6BT, United Kingdom
^{40} Center for Neutrino Physics, Virginia Tech, Blacksburg, VA, 24061, USA
^{41} University of Warwick, Coventry CV4 7AL, United Kingdom
^{42} Wright Laboratory, Department of Physics, Yale University, New Haven, CT, 06520, USA
(Dated: December 22, 2023)

We present a first search for dark-trident scattering in a neutrino beam using a data set corresponding to 7.2×10^{20} protons on target taken with the MicroBooNE detector at Fermilab. Proton interactions in the neutrino target at the Main Injector produce π^0 and η mesons, which could decay into dark-matter (DM) particles mediated via a dark photon A'. A convolutional neural network is trained to identify interactions of the DM particles in the liquid-argon time projection chamber (LArTPC) exploiting its image-like reconstruction capability. In the absence of a DM signal, we provide limits at the 90% confidence level on the squared kinematic mixing parameter ε^2 as a function of the dark-photon mass in the range $10 \leq M_{A'} \leq 400$ MeV. The limits cover previously unconstrained parameter space for the production of fermion or scalar DM particles χ for two benchmark models with mass ratios $M_\chi/M_{A'} = 0.6$ and 2 and for dark fine-structure constants $0.1 \leq \alpha_D \leq 1$.

A wealth of astronomical data at different scales provide evidence for the existence of dark matter (DM): the motion of galaxies and the stars within them, gravitational lensing, the cosmic microwave background, and the large-scale structure of the universe [1]. The nature of dark matter, however, remains elusive. Non-baryonic particles predicted by dark-sector models are candidates for dark matter [2]. The search for their production at accelerators is a focus of the high-energy hadron collider program at the LHC [3] and of fixed-target experiments exposed to high-intensity beams [4].

The dark-trident process has been proposed as a new way to search for low-mass dark-matter particles in neutrino beams [5]. In this letter, we report a first search for such dark tridents with the MicroBooNE liquid-argon time projection chamber (LArTPC) [6]. In the future, similar searches can be performed with the DUNE near detector [7] and the detectors of the Fermilab short-baseline program [8].

A pair of DM particles, $\chi\bar{\chi}$, is produced in the dark-trident process through the decay of neutral π^0 or η mesons, which was created by the interactions of the protons and by secondary interactions in the neutrino target (Fig. 1a). The decays $\pi^0, \eta \to \gamma\chi\bar{\chi}$ are mediated by a virtual, off-shell dark photon A'^*. The masses of the dark photon, $M_{A'}$, and of the dark fermion (or scalar), M_χ, are parameters of the model.

The DM particle χ (or $\bar{\chi}$) then travels uninterrupted to the MicroBooNE detector where it could scatter off argon nuclei through the trident process $\chi + \text{Ar} \to \chi + \text{Ar} + A'$ (see Fig. 1b). The dark photon A' promptly decays inside the detector into an e^+e^- pair. The χ production
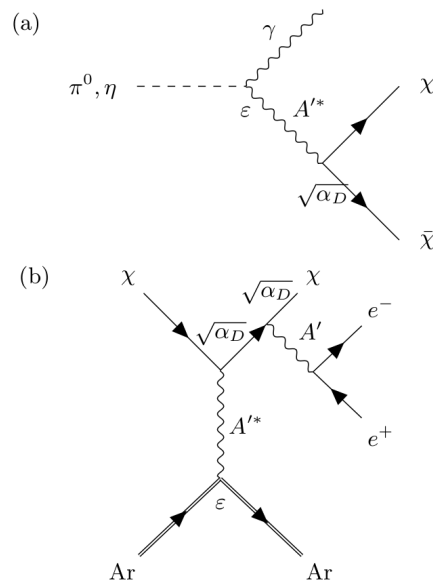

FIG. 1. (a) A pair of DM particles, $\chi\bar{\chi}$, is produced in a π^0 or η^0 decay; (b) in the dark-trident process, χ (or $\bar{\chi}$) scatters off an argon nucleus to produce a dark photon A' decaying into an e^+e^- pair with a branching ratio of 1. The rate depends on the kinematic mixing parameter ε and the dark fine-structure constant α_D.

rate depends on the kinematic mixing parameter ε and a dark fine-structure constant α_D, which is defined in terms of the dark-photon gauge coupling g_D as $\alpha_D = g_D^2/(4\pi)$. We consider the mass ratios $M_\chi/M_{A'} = 0.6$ and 2 in this search as proposed in Ref. [5]. Since $M_\chi/M_{A'} > 0.5$, the dark photons need to be off-shell to decay into $\chi\bar{\chi}$ pairs, and, when on-shell, they will exclusively decay to

e^+e^-. The signal rate therefore scales with $\varepsilon^4\alpha_D^3$. Other recent experimental searches cover the mass range where A' decays invisibly [9–11].

We use data recorded with the MicroBooNE detector [6] between 2015 and 2018. The detector's LArTPC has an instrumented volume of 85 tonnes of liquid argon inside a cryostat. Ionization charge drifts across an electric field of 273 V/cm and is read out by one charge collection and two induction planes forming the anode. The LArTPC was simultaneously exposed to the on-axis booster neutrino beam (BNB) [12] and the off-axis beam of neutrinos from the main injector (NuMI) [13]. Only NuMI data are used in this search, as the higher average energy of the NuMI beam gives access to higher values of $M_{A'}$.

The NuMI data used here correspond to 7.2×10^{20} protons on target (POT), which were taken in two operating modes – forward horn current (FHC) with 2.2×10^{20} POT (Run 1) and reverse horn current (RHC) with 5.0×10^{20} POT (Run 3). This data set has previously been used to search for heavy neutral leptons [14, 15] and Higgs portal scalars [15, 16], and to measure neutrino cross sections [17, 18].

We simulate the dark-trident process with a dedicated generator in three steps: the neutral meson flux in the beamline, the decay of the neutral mesons, and the scattering of the DM particles on argon. First, the kinematics of the π^0 and η mesons for both beam configurations, FHC and RHC, are obtained using the `g4NuMI` simulation [19], which is based on a full `GEANT4` description of the beamline geometry. The full simulation results in a significantly higher meson rate compared to Ref. [5] since it includes mesons produced within the ≈ 1 m long graphite target by secondary interactions and within other beamline components.

We then simulate the radiative decays $\pi^0, \eta^0 \to \gamma\chi\bar{\chi}$ with `BdNMC` [20]. In addition to the scalar DM production supported by `BdNMC`, we added the option to generate fermions. We calculate the rate of the scattering process $\chi + \text{Ar} \to \chi + \text{Ar} + A'$ inside the LArTPC as a function of the energy of the DM particle and the path traveled inside the detector [21]. We compare our signal simulation to the calculations of Ref. [5] and find good agreement in the kinematics, e.g., the distribution of the e^+e^- opening angle as a function of the energy of each lepton. The cross section of the process shown in Fig. 1b is calculated using `GenExLight` [21]. We find an agreement better than 1% when comparing these cross sections to calculations obtained with `MadGraph` [22].

We use a "beam-on" data sample to search for the dark-trident signal where the event triggers coincide with the arrival time of neutrinos from the NuMI beam. The background is modeled considering three contributions. Beam-on background events that are triggered by a cosmic ray and not a neutrino interaction are modeled by a "beam-off" sample collected under identical trigger conditions but when no neutrino beam is present. The "beam-off" sample is scaled so that its normalization corresponds to the number of beam spills of the beam-on sample. Neutrino-induced background from the NuMI beam is modeled using a `GENIE` Monte Carlo simulation [23] embedded in the `LArSoft` software framework [24]. The "in-cryostat ν" sample contains interactions of neutrinos with the argon inside the cryostat, and the "out-of-cryostat ν" sample describes interactions with the material surrounding the detector.

We reconstruct neutrino interactions and cosmic rays within the argon with a chain of pattern-recognition algorithms, implemented using the `Pandora` software development kit [25, 26]. The algorithms use hits that are formed from the waveforms read out by the charge collection plane and the two induction planes. Collections of hits are reconstructed as a track, as expected for a minimum ionizing particle, or a shower, consistent with being an electron or photon conversion.

TABLE I. Numbers of events that remain after preselection normalized to POT for the data and the background model.

Sample	Run 1 (FHC)	Run 3 (RHC)
POT	2.2×10^{20}	5.0×10^{20}
Beam-off	2410	4826
In-cryostat ν	1262	2759
Out-of-cryostat ν	354	402
Sum of predictions	4026	7987
Beam-on (data)	4021	7684

We use the results of the `Pandora` reconstruction to select events that are consistent with the signal hypothesis. Dark-trident events are frequently reconstructed as a single shower due to the small opening angle of the e^+e^- pairs and, in a few cases, as two showers arising from a common vertex. Background processes that can mimic the signal topology are neutral current (NC) ν interactions with $\pi^0, \eta \to \gamma\gamma$ decays in the final state or with emission of single photons that are reconstructed as an e^+e^- pair. Each event is therefore required to have at least one vertex, at least one shower, and no tracks. The efficiency of this preselection for a DM signal lies in the range of (32–40)% for masses in the range (10–400) MeV. We find good agreement between the number of data events and the sum of the predictions for the background processes after this preselection (Table I).

We use a convolutional neural network (CNN) for discriminating signal and background based on the previous development of such algorithms in MicroBooNE for multiple particle identification (MPID) [27]. Convolutional neural networks (CNNs) are deep learning networks that are ideally suited for images reconstructed from LArTPC data [28–30]. The CNN architecture is based on a model for dense images with adaptations for LArTPCs. Convolution filters of size 3×3 allow scanning of the information contained in showers. The output layer has two

neurons that correspond to the probability for signal or background.

We only consider images from the charge collection plane, as it has the best signal to noise ratio [27]. The size of each image in pixels corresponds to 3456 wires multiplied by 6048 time ticks. To improve processing time, we first compress the time axis by a factor of 6 and then crop the images around the interaction vertex producing a region of interest (ROI) of 512×512 pixels. After compression, each pixel has a resolution of $\approx 3 \times 3$ mm^2.
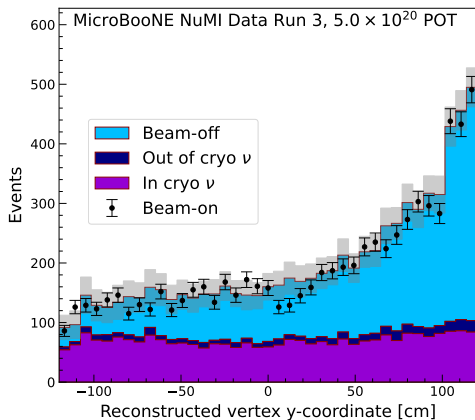

FIG. 2. Distribution of the y coordinate of the reconstructed vertices for the Run 3 data after preselection compared to the background model. The positive direction of the y axis points vertically upwards. The gray band represents the systematic uncertainty in the background model.

We validate the agreement of the vertex reconstruction by comparing data and the background model after the preselection (Fig. 2). The increase of beam-off events towards the top of the detector due to cosmic rays is reproduced by the background model. While we use the reconstructed vertices for the data and background samples, the true vertex location is used for the training. This prevents the CNN from training on an ROI that does not contain the interaction of interest, which can occur when a vertex is reconstructed at a large distance from the true interaction vertex.

For the training of the CNN we prepare a dedicated training data set. We use a single signal sample with the parameters $\alpha_D = 0.1$, $M_{A'} = 50$ MeV, and $M_{A'}/M_\chi = 0.6$. As background samples we use cosmic rays simulated with `CORSIKA` [31] and ν interactions leading to π^0 mesons simulated with `GENIE` [23]. In addition, we overlay the hits of cosmic rays simulated with `CORSIKA` to the ν interaction background and the signal samples. A test set, comprising 10% of the events included in the training set, is used to evaluate the progress of the CNN training.

The CNN model is trained during $\approx 10{,}000$ iterations (≈ 5 epochs) with a batch size of 32 images and a learning rate of 0.001 [28]. Dropout layers, regularization
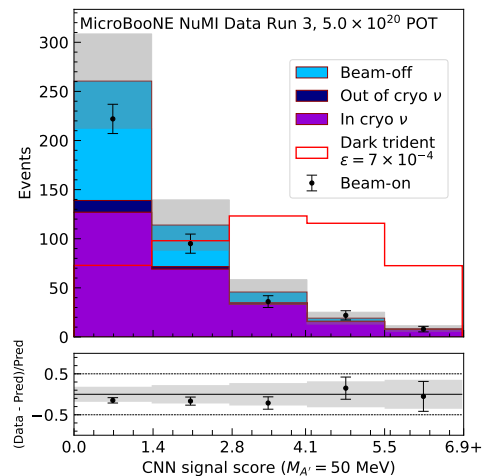

FIG. 3. Comparison of the CNN signal score distribution for Run 3 data with the background model after the preselection. The gray band corresponds to the total systematic uncertainty in the background. The signal distribution for $\alpha_D = 0.1$, $M_{A'} = 50$ MeV, and $M_{A'}/M_\chi = 0.6$ is superimposed, scaled by an arbitrary factor.
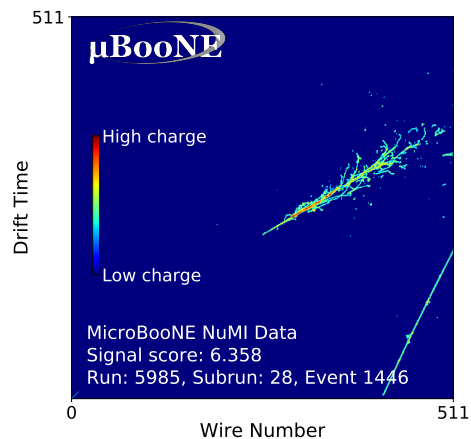

FIG. 4. A dark-trident candidate with a CNN score of 6.4, within the ROI of 512×512 pixels ($\approx 1.5 \times 1.5$ m^2). A cosmic ray crosses in the lower right-hand corner.

terms, and batch normalization are implemented during the CNN training to prevent overfitting. The training progress is monitored with a Binary Cross Entropy (BCE) loss function and using the accuracy, which is defined as the fraction of correctly classified images over the total number of images processed by the CNN. As an additional figure of merit, we use the receiver operating characteristic curve (ROC) to decide the number of training steps where the CNN model is frozen. Figure 3 shows the discrimination between signal and background for CNN signal scores > 0.

We use a single CNN model that has been optimized with a benchmark signal point trained against the NC π^0 and cosmic-ray background samples. The areas under the
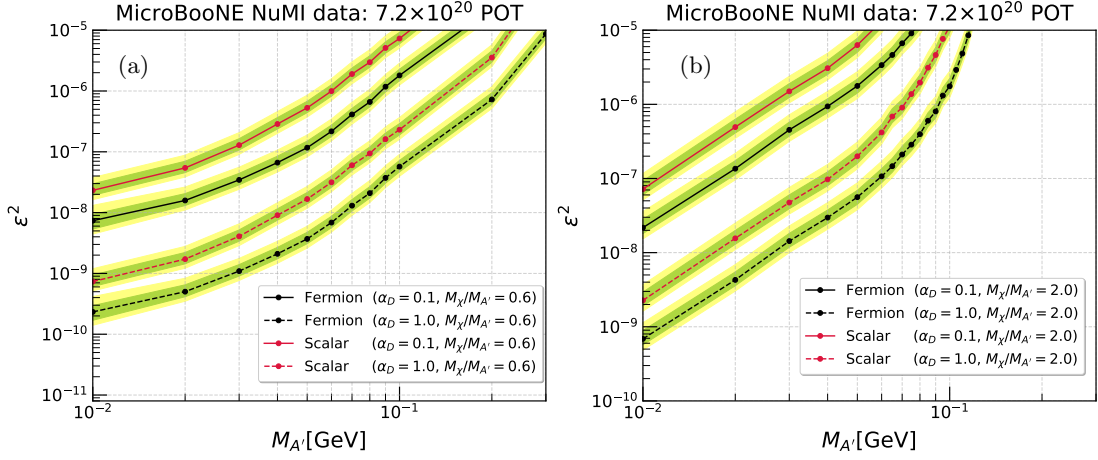
FIG. 5. The 90% CL observed limits on ε^2 as a function of $M_{A'}$ for $\alpha_D = 0.1$ and $\alpha_D = 1$, and (a) $M_\chi/M_{A'} = 0.6$ and (b) $M_\chi/M_{A'} = 2$, together with the 1 and 2 standard deviation bands around the median expected limits. We use a linear interpolation between the mass points. A total of 13 mass values have been simulated for $M_\chi/M_{A'} = 0.6$, equally spaced between 10–100 MeV and between 100–400 MeV and a total of 19 mass values for $M_\chi/M_{A'} = 2$, an additional 6 mass values are added at higher M_A. A table of the limits at each point is provided as supplementary material.
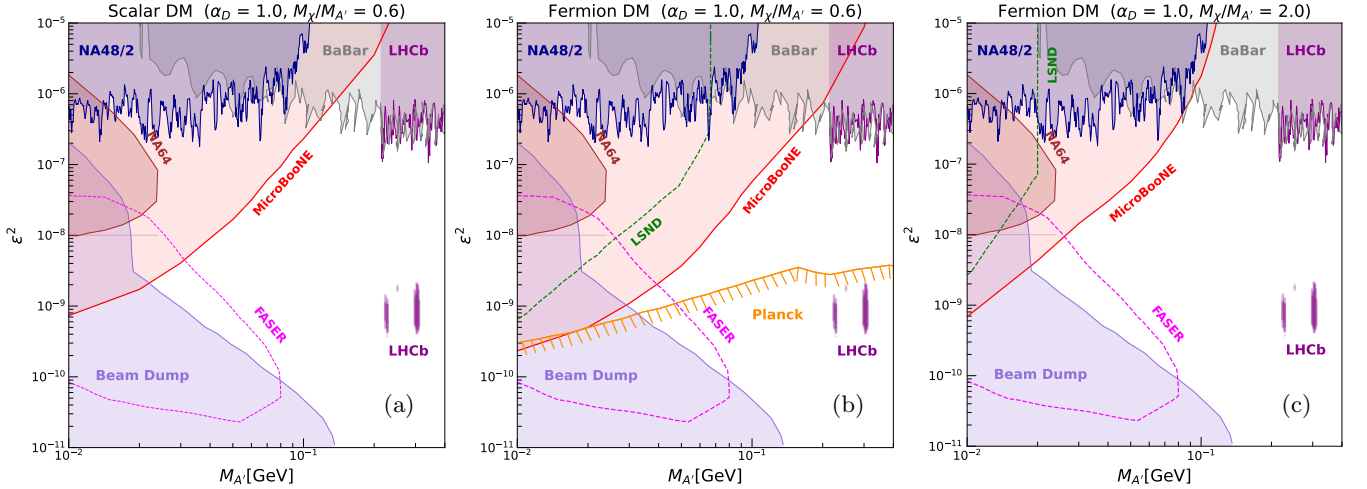

FIG. 6. The 90% CL limits on ε^2 as a function of $M_{A'}$ for (a) scalar DM with $\alpha_D = 1.0$, $M_\chi/M_{A'} = 0.6$; (b) fermion DM with $\alpha_D = 1.0$, $M_\chi/M_{A'} = 0.6$; and (c) for fermion DM with $\alpha_D = 1.0$, $M_\chi/M_{A'} = 2.0$. The constraints provided by the NA48/2 [32], BaBar [33], NA64 [34], and LHCb collaborations [35], and by beam dump experiments [36–38] are displayed as shaded regions. The reinterpretations of LSND results [5, 39] and the unpublished FASER [40] limits are shown as dashed lines. The two isolated contours at $M_{A'} \approx 200$–300 MeV are also excluded by LHCb data. The upper limits on ε^2 from Planck data [41, 42] apply for fermion DM with $M_\chi/M_{A'} = 0.6$.

curve for the ROCs of the different signal points relative to the full background sample (see Table I) agree within (1–2)% with the benchmark CNN model.

A data event with a high CNN signal score is shown in Fig. 4, where the shower points in the direction of the NuMI beam. By modifying the training events, we determine that the CNN learns about the kinematics (angles, energies) of the scattering process through the number of pixels and the orientation of pixel clusters.

We evaluate systematic uncertainties that could modify the CNN score distributions for signal and back-

ground. For the in-cryostat ν background, we consider the impact of the neutrino flux simulation (10–20)% [19], the neutrino-argon cross-section modeling (12–20)% [43], hadron interactions with argon ($\approx$ 1%) [44], and detector modeling ($\approx$ 30%) [45]. The beam-off sample is taken from data and therefore has no associated systematic uncertainties other than statistical fluctuations. The impact of the normalization uncertainty on the out-of-cryostat sample and of the POT counting is negligible [15].

The sum of the detector-related systematic uncertain-

ties on the signal is in the range (10–20)%. A form factor accounts for the spatial distribution of the argon nucleus in the χ-Ar scattering [5]. Recalculating the cross sections with different form factors [46, 47] yields uncertainties in the range (2–20)% in the mass range (10–200) MeV.

The signal rate also depends on the NuMI π^0 and η flux simulated by `g4NuMI`. We confirm that the ratio of π^0 production relative to $\pi^{\pm}$ production in `g4NuMI` is consistent with expectations of isospin symmetry. We therefore use the beam flux uncertainty of 22% determined for the charged meson flux [17], which includes hadron production and beam line modeling uncertainties.

The CNN score distributions are found to be consistent with the background expectation and used to derive limits on the squared mixing parameter ε^2 as a function of $M_{A'}$. The limit setting is done with the `pyhf` algorithm [48], which is an implementation of a statistical model to estimate confidence intervals [49]. Systematic uncertainties are treated through profile likelihood ratios. The results are validated with the modified frequentist CL_s calculation of the `COLLIE` program [50].

The observed limits of Fig. 5 are shown at the 90% confidence level ($\mathrm{CL}_s = 0.1$) for several benchmark points. Since we use a single CNN model for all signal points, the background CNN score distributions are highly correlated between the different mass hypotheses $M_{A'}$. All observed limits are therefore consistently within the 1 and 2 standard deviation ranges around the median expected limit.

In Fig. 6, we compare the results for a scalar dark matter particle χ with existing constraints on dark-trident processes from rare pion decays measured by the NA48/2 collaboration [32], beam dump experiments [36–38], and searches for promptly decaying dark photons into e^+e^- pairs by the BaBar [33], FASER [40], and NA64 [51] collaborations. The limits obtained by the LHCb collaboration [35] apply for higher masses $M_{A'} > 200$ MeV. The most sensitive constraints are obtained for $\alpha_D = 1$ and $M_\chi/M_{A'} = 0.6$.

For the fermion model, we also compare to reinterpretations of LSND results [5, 39]. Cosmological constraints on $\chi\bar{\chi}$ annihilation in the early universe are obtained using Planck measurements on the cosmic microwave background [41, 42]. The $\chi\bar{\chi}$ annihilation cross section is only relevant for a fermion χ and $M_\chi/M_{A'} = 0.6$. The cosmological data constrain ε^2 from below, since the thermal relic dark-matter density becomes too small for larger ε^2 [5].

In summary, we apply convolutional neural networks to obtain first constraints on the production of dark matter in a liquid argon detector exposed to a neutrino beam. We consider fermion and boson dark-matter particles χ produced in a dark-trident process with $M_\chi/M_{A'} = 0.6$ and $M_\chi/M_{A'} = 2$, and dark fine-structure constants in the range $0.1 \leq \alpha_D \leq 1$. The constraints in the plane of the squared kinematic mixing parameter ε^2 and the dark-photon mass $M_{A'}$ exclude previously unexplored regions of parameter space in the range $10 \leq M_{A'} \leq 400$ MeV.

---

* microboone_info@fnal.gov

[1] N. Aghanim *et al.* (Planck Collaboration), Planck 2018 results. VI. Cosmological parameters, Astron. Astrophys. **641**, A6 (2020), [Erratum: Astron.Astrophys. 652, C4 (2021)].

[2] A. Arbey and F. Mahmoudi, Dark matter and the early Universe: a review, Prog. Part. Nucl. Phys. **119**, 103865 (2021).

[3] T. G. Rizzo, Portal Matter and Dark Sector Phenomenology at Colliders, in *Snowmass 2021* (2022) arXiv:2202.02222 [hep-ph].

[4] C. Antel *et al.*, Feebly-interacting particles: FIPs 2022 Workshop Report, Eur. Phys. J. C **83**, 1122 (2023).

[5] A. de Gouvêa, P. J. Fox, R. Harnik, K. J. Kelly, and Y. Zhang, Dark Tridents at Off-Axis Liquid Argon Neutrino Detectors, J. High Energy Phys. **01**, 001.

[6] R. Acciarri *et al.* (MicroBooNE Collaboration), Design and construction of the MicroBooNE detector, J. Instrum. **12** (02), P02017.

[7] B. Abi *et al.* (DUNE Collaboration), Prospects for beyond the Standard Model physics searches at the Deep Underground Neutrino Experiment, Eur. Phys. J. C **81**, 322 (2021).

[8] P. A. Machado, O. Palamara, and D. W. Schmitz, The Short-Baseline Neutrino Program at Fermilab, Ann. Rev. Nucl. Part. Sci. **69** (2019).

[9] A. Aguilar-Arevalo *et al.* (MiniBooNE-DM Collaboration), Dark matter search in nucleon, pion, and electron channels from a proton beam dump with MiniBooNE, Phys. Rev. D **98**, 112004 (2018).

[10] D. Akimov *et al.* (COHERENT Collaboration), First probe of sub-gev dark matter beyond the cosmological expectation with the COHERENT CsI detector at the SNS, Phys. Rev. Lett. **130**, 051803 (2023).

[11] Y. M. Andreev *et al.* (NA64 Collaboration), Search for Light Dark Matter with NA64 at CERN, Phys. Rev. Lett. **131**, 161801 (2023).

[12] A. A. Aguilar-Arevalo *et al.* (MiniBooNE Collaboration), The neutrino flux prediction at MiniBooNE, Phys. Rev. **D79**, 072002 (2009).

[13] P. Adamson *et al.*, The NuMI neutrino beam, Nucl. Instrum. Meth. **A806**, 279 (2016).

[14] P. Abratenko *et al.* (MicroBooNE Collaboration), Search for heavy neutral leptons in electron-positron and neutral-pion final states with the MicroBooNE detector, (2023), accepted by Phys. Rev. Lett., arXiv:2310.07660 [hep-ex].

[15] P. Abratenko *et al.* (MicroBooNE Collaboration), Search for long-lived heavy neutral leptons and Higgs portal scalars decaying in the MicroBooNE detector, Phys. Rev. D **106**, 092006 (2022).

[16] P. Abratenko *et al.* (MicroBooNE Collaboration), Search for a Higgs Portal Scalar Decaying to Electron-Positron Pairs in the MicroBooNE Detector, Phys. Rev. Lett. **127**, 151803 (2021).

[17] P. Abratenko *et al.* (MicroBooNE Collaboration), Measurement of the flux-averaged inclusive charged-current electron neutrino and antineutrino cross section on argon using the NuMI beam and the MicroBooNE detector, Phys. Rev. D **104**, 052002 (2021).

[18] P. Abratenko *et al.* (MicroBooNE Collaboration), First measurement of inclusive electron-neutrino and antineutrino charged current differential cross sections in charged lepton energy on argon in MicroBooNE, Phys. Rev. D **105**, L051102 (2022).

[19] L. Aliaga *et al.* (MINERvA Collaboration), Neutrino Flux Predictions for the NuMI Beam, Phys. Rev. D **94**, 092005 (2016), [Addendum: Phys. Rev. D 95, 039903 (2017)].

[20] P. deNiverville, C.-Y. Chen, M. Pospelov, and A. Ritz, Light dark matter in neutrino beams: production modelling and scattering signatures at MiniBooNE, T2K and SHiP, Phys. Rev. D **95**, 035006 (2017).

[21] R. A. Kycia, J. Turnau, J. J. Chwastowski, R. Staszewski, and M. Trzebiński, The adaptive Monte Carlo toolbox for phase space integration and generation, Commun. Comput. Phys. **25**, 1547 (2019).

[22] J. Alwall, R. Frederix, S. Frixione, V. Hirschi, F. Maltoni, O. Mattelaer, H. S. Shao, T. Stelzer, P. Torrielli, and M. Zaro, The automated computation of tree-level and next-to-leading order differential cross sections, and their matching to parton shower simulations, J. High. Energy Phys. **07**, 079 (2014).

[23] C. Andreopoulos, C. Barry, S. Dytman, H. Gallagher, T. Golan, R. Hatcher, G. Perdue, and J. Yarba, The GENIE Neutrino Monte Carlo Generator: Physics and User Manual, (2015), arXiv:1510.05494 [hep-ph].

[24] E. L. Snider and G. Petrillo, LArSoft: Toolkit for Simulation, Reconstruction and Analysis of Liquid Argon TPC Neutrino Detectors, J. Phys. Conf. Ser. **898**, 042057 (2017).

[25] J. S. Marshall and M. A. Thomson, The Pandora Software Development Kit for Pattern Recognition, Eur. Phys. J. **C75**, 439 (2015).

[26] R. Acciarri *et al.* (MicroBooNE Collaboration), The Pandora multi-algorithm approach to automated pattern recognition of cosmic-ray muon and neutrino events in the MicroBooNE detector, Eur. Phys. J. C **78**, 82 (2018), we use v03_14_04_01 of the Pandora LArTPC algorithms.

[27] P. Abratenko *et al.* (MicroBooNE Collaboration), Convolutional neural network for multiple particle identification in the MicroBooNE liquid argon time projection chamber, Phys. Rev. D **103**, 092003 (2021).

[28] R. Acciarri *et al.* (MicroBooNE Collaboration), Convolutional Neural Networks Applied to Neutrino Events in a Liquid Argon Time Projection Chamber, J. Instrum. **12** (03), P03011.

[29] P. Abratenko *et al.* (MicroBooNE Collaboration), Cosmic ray muon clustering for the MicroBooNE liquid argon time projection chamber using sMask-RCNN, J. Instrum. **17** (09), P09015.

[30] P. Abratenko *et al.* (MicroBooNE Collaboration), First demonstration for a LArTPC-based search for intranuclear neutron-antineutron transitions and annihilation in ^{40}Ar using the MicroBooNE detector, (2023), arXiv:2308.03924 [hep-ex].

[31] D. Heck *et al.*, CORSIKA: A Monte Carlo code to simulate extensive air showers, *CORSIKA: A Monte Carlo code to simulate extensive air showers*, FZKA-6019 (1998).

[32] J. R. Batley *et al.* (NA48/2 Collaboration), Search for the dark photon in π^0 decays, Phys. Lett. B **746**, 178 (2015).

[33] J. P. Lees *et al.* (BaBar Collaboration), Search for a Dark Photon in e^+e^- Collisions at BaBar, Phys. Rev. Lett. **113**, 201801 (2014).

[34] D. Banerjee *et al.* (The NA64 Collaboration), Improved limits on a hypothetical $x(16.7)$ boson and a dark photon decaying into e^+e^- pairs, Phys. Rev. D **101**, 071101 (2020).

[35] R. Aaij *et al.* (LHCb Collaboration), Search for Dark Photons Produced in 13 TeV pp Collisions, Phys. Rev. Lett. **120**, 061801 (2018).

[36] J. D. Bjorken, S. Ecklund, W. R. Nelson, A. Abashian, C. Church, B. Lu, L. W. Mo, T. A. Nunamaker, and P. Rassmann, Search for Neutral Metastable Penetrating Particles Produced in the SLAC Beam Dump, Phys. Rev. D **38**, 3375 (1988).

[37] E. M. Riordan *et al.*, A Search for Short Lived Axions in an Electron Beam Dump Experiment, Phys. Rev. Lett. **59**, 755 (1987).

[38] A. Bross, M. Crisler, S. H. Pordes, J. Volk, S. Errede, and J. Wrbanek, A Search for Shortlived Particles Produced in an Electron Beam Dump, Phys. Rev. Lett. **67**, 2942 (1991).

[39] Y. Kahn, G. Krnjaic, J. Thaler, and M. Toups, DAEδALUS and dark matter detection, Phys. Rev. D **91**, 055006 (2015).

[40] J. Boyd *et al.* (FASER Collaboration), First Results from the Search for Dark Photons with the FASER Detector at the LHC, (2023), CERN-FASER-CONF-2023-001.

[41] M. S. Madhavacheril, N. Sehgal, and T. R. Slatyer, Current Dark Matter Annihilation Constraints from CMB and Low-Redshift Data, Phys. Rev. D **89**, 103508 (2014).

[42] T. R. Slatyer, Indirect dark matter signatures in the cosmic dark ages. I. Generalizing the bound on s-wave dark matter annihilation from Planck results, Phys. Rev. D **93**, 023527 (2016).

[43] P. Abratenko *et al.* (MicroBooNE Collaboration), New CC0π GENIE model tune for MicroBooNE, Phys. Rev. D **105**, 072001 (2022).

[44] J. Calcutt, C. Thorpe, K. Mahn, and L. Fields, Geant4reweight: a framework for evaluating and propagating hadronic interaction uncertainties in geant4, Journal of Instrumentation **16** (08), P08042.

[45] P. Abratenko *et al.* (MicroBooNE Collaboration), Novel approach for evaluating detector-related uncertainties in a LArTPC using MicroBooNE data, Eur. Phys. J. C **82**, 454 (2022).

[46] H. De Vries, C. W. De Jager, and C. De Vries, Nuclear charge and magnetization density distribution parameters from elastic electron scattering, Atom. Data Nucl. Data Tabl. **36**, 495 (1987).

[47] G. Duda, A. Kemper, and P. Gondolo, Model Independent Form Factors for Spin Independent Neutralino-Nucleon Scattering from Elastic Electron Scattering Data, JCAP **04**, 012.

[48] L. Heinrich, M. Feickert, G. Stark, and K. Cranmer, pyhf: pure–python implementation of histfactory statistical models, Journal of Open Source Software **6**, 2823 (2021).

[49] G. Cowan, K. Cranmer, E. Gross, and O. Vitells, Asymptotic formulae for likelihood-based tests of new physics, Eur. Phys. J. C **71**, 1554 (2011), [Erratum: Eur. Phys. J. C 73, 2501 (2013)].

[50] W. Fisher (DØ Collaboration), Systematics and limit calculations, FERMILAB-TM-2386-E, 10.2172/923070 (2006).

[51] Y. M. Andreev *et al.* (NA64 Collaboration), Search for pseudoscalar bosons decaying into e^+e^- pairs in the NA64 experiment at the CERN SPS, Phys. Rev. D **104**, L111102 (2021).

Supplemental material: first search for dark-trident processes using the MicroBooNE detector
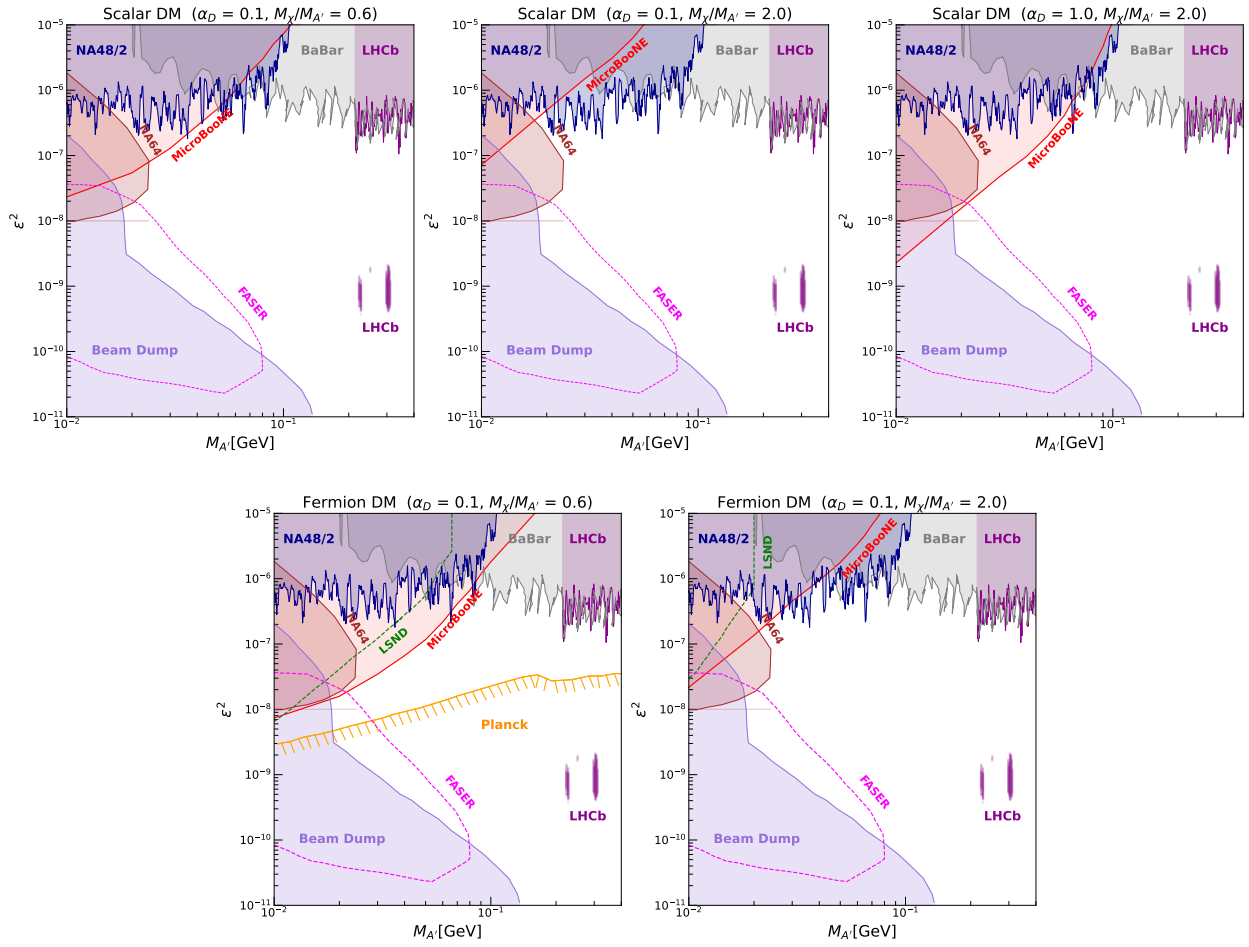
FIG. 7. The 90% CL limits on ε^2 as a function of $M_{A'}$. The first row corresponds to scalar DM models and the second row to fermion DM models. The constraints provided by the NA48/2 [32], BaBar [33], NA64 [51], and LHCb collaborations [35], and by beam dump experiments [36–38] are displayed as shaded regions. The reinterpretations of LSND results [5, 39] and the unpublished FASER [40] limits are shown as dashed lines. The two isolated contours at $M_{A'} \approx 200$–300 MeV are also excluded by LHCb data. The upper limits on ε^2 from Planck data [41, 42] apply for fermion DM with $M_\chi/M_{A'} = 0.6$.

Scalar Dark Matter, $\alpha_D = 0.1$, $M_\chi/M_{A'} = 2.0$

$M_{A'}$ (MeV)	Observed	Expected	Expected 1σ	Expected 2σ
10	$7.19 \cdot 10^{-8}$	$7.40 \cdot 10^{-8}$	$(6.04\text{--}9.29) \cdot 10^{-8}$	$(0.51\text{--}1.17) \cdot 10^{-7}$
20	$4.93 \cdot 10^{-7}$	$5.01 \cdot 10^{-7}$	$(4.10\text{--}6.30) \cdot 10^{-7}$	$(3.47\text{--}7.92) \cdot 10^{-7}$
30	$1.50 \cdot 10^{-6}$	$1.51 \cdot 10^{-6}$	$(1.24\text{--}1.90) \cdot 10^{-6}$	$(1.05\text{--}2.39) \cdot 10^{-6}$
40	$3.07 \cdot 10^{-6}$	$3.09 \cdot 10^{-6}$	$(2.53\text{--}3.89) \cdot 10^{-6}$	$(2.14\text{--}4.89) \cdot 10^{-6}$
50	$6.30 \cdot 10^{-6}$	$6.18 \cdot 10^{-6}$	$(5.04\text{--}7.78) \cdot 10^{-6}$	$(4.26\text{--}9.81) \cdot 10^{-6}$
60	$1.32 \cdot 10^{-5}$	$1.33 \cdot 10^{-5}$	$(1.09\text{--}1.68) \cdot 10^{-5}$	$(0.92\text{--}2.11) \cdot 10^{-5}$
65	$2.17 \cdot 10^{-5}$	$2.19 \cdot 10^{-5}$	$(1.80\text{--}2.76) \cdot 10^{-5}$	$(1.52\text{--}3.47) \cdot 10^{-5}$
70	$2.86 \cdot 10^{-5}$	$2.92 \cdot 10^{-5}$	$(2.39\text{--}3.67) \cdot 10^{-5}$	$(2.02\text{--}4.62) \cdot 10^{-5}$
75	$4.35 \cdot 10^{-5}$	$4.38 \cdot 10^{-5}$	$(3.58\text{--}5.51) \cdot 10^{-5}$	$(3.03\text{--}6.93) \cdot 10^{-5}$
80	$6.21 \cdot 10^{-5}$	$6.28 \cdot 10^{-5}$	$(5.13\text{--}7.90) \cdot 10^{-5}$	$(4.34\text{--}9.95) \cdot 10^{-5}$
85	$9.87 \cdot 10^{-5}$	$1.01 \cdot 10^{-4}$	$(0.82\text{--}1.26) \cdot 10^{-4}$	$(0.70\text{--}1.59) \cdot 10^{-4}$
90	$1.46 \cdot 10^{-4}$	$1.47 \cdot 10^{-4}$	$(1.20\text{--}1.84) \cdot 10^{-4}$	$(1.01\text{--}2.32) \cdot 10^{-4}$
95	$2.41 \cdot 10^{-4}$	$2.45 \cdot 10^{-4}$	$(2.00\text{--}3.08) \cdot 10^{-4}$	$(1.69\text{--}3.88) \cdot 10^{-4}$
100	$3.55 \cdot 10^{-4}$	$3.59 \cdot 10^{-4}$	$(2.93\text{--}4.51) \cdot 10^{-4}$	$(2.49\text{--}5.67) \cdot 10^{-4}$
105	$5.74 \cdot 10^{-4}$	$5.80 \cdot 10^{-4}$	$(4.74\text{--}7.29) \cdot 10^{-4}$	$(4.02\text{--}9.18) \cdot 10^{-4}$
110	$1.19 \cdot 10^{-3}$	$1.22 \cdot 10^{-3}$	$(1.00\text{--}1.53) \cdot 10^{-3}$	$(0.84\text{--}1.93) \cdot 10^{-3}$
115	$2.18 \cdot 10^{-3}$	$2.19 \cdot 10^{-3}$	$(1.79\text{--}2.76) \cdot 10^{-3}$	$(1.52\text{--}3.48) \cdot 10^{-3}$
120	$5.63 \cdot 10^{-3}$	$5.69 \cdot 10^{-3}$	$(4.65\text{--}7.15) \cdot 10^{-3}$	$(3.94\text{--}9.00) \cdot 10^{-3}$
125	$1.74 \cdot 10^{-2}$	$1.80 \cdot 10^{-2}$	$(1.47\text{--}2.27) \cdot 10^{-2}$	$(1.25\text{--}2.86) \cdot 10^{-2}$

Scalar Dark Matter, $\alpha_D = 1.0$, $M_\chi/M_{A'} = 2.0$

$M_{A'}$ (MeV)	Observed	Expected	Expected 1σ	Expected 2σ
10	$2.27 \cdot 10^{-9}$	$2.34 \cdot 10^{-9}$	$(1.91\text{--}2.94) \cdot 10^{-9}$	$(1.62\text{--}3.69) \cdot 10^{-9}$
20	$1.56 \cdot 10^{-8}$	$1.59 \cdot 10^{-8}$	$(1.30\text{--}1.99) \cdot 10^{-8}$	$(1.10\text{--}2.51) \cdot 10^{-8}$
30	$4.74 \cdot 10^{-8}$	$4.79 \cdot 10^{-8}$	$(3.91\text{--}6.02) \cdot 10^{-8}$	$(3.31\text{--}7.57) \cdot 10^{-8}$
40	$9.71 \cdot 10^{-8}$	$9.77 \cdot 10^{-8}$	$(0.80\text{--}1.23) \cdot 10^{-7}$	$(0.68\text{--}1.55) \cdot 10^{-7}$
50	$1.99 \cdot 10^{-7}$	$1.95 \cdot 10^{-7}$	$(1.59\text{--}2.46) \cdot 10^{-7}$	$(1.35\text{--}3.10) \cdot 10^{-7}$
60	$4.18 \cdot 10^{-7}$	$4.21 \cdot 10^{-7}$	$(3.44\text{--}5.30) \cdot 10^{-7}$	$(2.91\text{--}6.67) \cdot 10^{-7}$
65	$6.85 \cdot 10^{-7}$	$6.94 \cdot 10^{-7}$	$(5.68\text{--}8.73) \cdot 10^{-7}$	$(0.48\text{--}1.10) \cdot 10^{-6}$
70	$9.04 \cdot 10^{-7}$	$9.24 \cdot 10^{-7}$	$(0.75\text{--}1.16) \cdot 10^{-6}$	$(0.64\text{--}1.46) \cdot 10^{-6}$
75	$1.37 \cdot 10^{-6}$	$1.38 \cdot 10^{-6}$	$(1.13\text{--}1.74) \cdot 10^{-6}$	$(0.96\text{--}2.19) \cdot 10^{-6}$
80	$1.96 \cdot 10^{-6}$	$1.99 \cdot 10^{-6}$	$(1.62\text{--}2.50) \cdot 10^{-6}$	$(1.37\text{--}3.15) \cdot 10^{-6}$
85	$3.12 \cdot 10^{-6}$	$3.18 \cdot 10^{-6}$	$(2.60\text{--}4.00) \cdot 10^{-6}$	$(2.20\text{--}5.03) \cdot 10^{-6}$
90	$4.63 \cdot 10^{-6}$	$4.63 \cdot 10^{-6}$	$(3.78\text{--}5.83) \cdot 10^{-6}$	$(3.21\text{--}7.33) \cdot 10^{-6}$
95	$7.63 \cdot 10^{-6}$	$7.74 \cdot 10^{-6}$	$(6.32\text{--}9.73) \cdot 10^{-6}$	$(0.54\text{--}1.23) \cdot 10^{-5}$
100	$1.12 \cdot 10^{-5}$	$1.14 \cdot 10^{-5}$	$(0.93\text{--}1.43) \cdot 10^{-5}$	$(0.79\text{--}1.79) \cdot 10^{-5}$
105	$1.82 \cdot 10^{-5}$	$1.84 \cdot 10^{-5}$	$(1.50\text{--}2.31) \cdot 10^{-5}$	$(1.27\text{--}2.90) \cdot 10^{-5}$
110	$3.75 \cdot 10^{-5}$	$3.85 \cdot 10^{-5}$	$(3.15\text{--}4.84) \cdot 10^{-5}$	$(2.67\text{--}6.09) \cdot 10^{-5}$
115	$6.88 \cdot 10^{-5}$	$6.94 \cdot 10^{-5}$	$(5.66\text{--}8.73) \cdot 10^{-5}$	$(0.48\text{--}1.10) \cdot 10^{-4}$
120	$1.78 \cdot 10^{-4}$	$1.80 \cdot 10^{-4}$	$(1.47\text{--}2.26) \cdot 10^{-4}$	$(1.25\text{--}2.85) \cdot 10^{-4}$
125	$5.50 \cdot 10^{-4}$	$5.71 \cdot 10^{-4}$	$(4.66\text{--}7.17) \cdot 10^{-4}$	$(3.95\text{--}9.03) \cdot 10^{-4}$

TABLE II. The 90% CL observed limits on ε^2 for a scalar DM particle χ as a function of $M_{A'}$ for $\alpha_D = 0.1$ and $\alpha_D = 1$, and $M_\chi/M_{A'} = 2$, together with the 1 and 2 standard deviation bands around the median expected limits. The results are obtained with a data set of 7.2×10^{20} POT.

Fermion Dark Matter, $\alpha_D = 0.1$, $M_\chi/M_{A'} = 2.0$

$M_{A'}$ (MeV)	Observed	Expected	Expected 1σ	Expected 2σ
10	$2.17 \cdot 10^{-8}$	$2.22 \cdot 10^{-8}$	$(1.81–2.82) \cdot 10^{-8}$	$(1.53–3.58) \cdot 10^{-8}$
20	$1.36 \cdot 10^{-7}$	$1.38 \cdot 10^{-7}$	$(1.13–1.74) \cdot 10^{-7}$	$(0.96–2.18) \cdot 10^{-7}$
30	$4.53 \cdot 10^{-7}$	$4.58 \cdot 10^{-7}$	$(3.74–5.75) \cdot 10^{-7}$	$(3.16–7.24) \cdot 10^{-7}$
40	$9.39 \cdot 10^{-7}$	$9.45 \cdot 10^{-7}$	$(0.77–1.19) \cdot 10^{-6}$	$(0.65–1.49) \cdot 10^{-6}$
50	$1.77 \cdot 10^{-6}$	$1.74 \cdot 10^{-6}$	$(1.42–2.19) \cdot 10^{-6}$	$(1.20–2.76) \cdot 10^{-6}$
60	$3.38 \cdot 10^{-6}$	$3.40 \cdot 10^{-6}$	$(2.78–4.28) \cdot 10^{-6}$	$(2.35–5.39) \cdot 10^{-6}$
65	$4.63 \cdot 10^{-6}$	$4.69 \cdot 10^{-6}$	$(3.84–5.90) \cdot 10^{-6}$	$(3.25–7.42) \cdot 10^{-6}$
70	$6.66 \cdot 10^{-6}$	$6.81 \cdot 10^{-6}$	$(5.56–8.56) \cdot 10^{-6}$	$(0.47–1.08) \cdot 10^{-5}$
75	$9.05 \cdot 10^{-6}$	$9.12 \cdot 10^{-6}$	$(0.75–1.15) \cdot 10^{-5}$	$(0.63–1.44) \cdot 10^{-5}$
80	$1.25 \cdot 10^{-5}$	$1.27 \cdot 10^{-5}$	$(1.04–1.59) \cdot 10^{-5}$	$(0.88–2.01) \cdot 10^{-5}$
85	$1.90 \cdot 10^{-5}$	$1.94 \cdot 10^{-5}$	$(1.58–2.44) \cdot 10^{-5}$	$(1.34–3.07) \cdot 10^{-5}$
90	$2.54 \cdot 10^{-5}$	$2.54 \cdot 10^{-5}$	$(2.07–3.19) \cdot 10^{-5}$	$(1.76–4.02) \cdot 10^{-5}$
95	$4.16 \cdot 10^{-5}$	$4.21 \cdot 10^{-5}$	$(3.44–5.30) \cdot 10^{-5}$	$(2.91–6.67) \cdot 10^{-5}$
100	$5.54 \cdot 10^{-5}$	$5.61 \cdot 10^{-5}$	$(4.58–7.04) \cdot 10^{-5}$	$(3.88–8.85) \cdot 10^{-5}$
105	$9.22 \cdot 10^{-5}$	$9.32 \cdot 10^{-5}$	$(0.76–1.17) \cdot 10^{-4}$	$(0.64–1.47) \cdot 10^{-4}$
110	$1.53 \cdot 10^{-4}$	$1.57 \cdot 10^{-4}$	$(1.29–1.98) \cdot 10^{-4}$	$(1.09–2.49) \cdot 10^{-4}$
115	$2.69 \cdot 10^{-4}$	$2.71 \cdot 10^{-4}$	$(2.21–3.41) \cdot 10^{-4}$	$(1.88–4.30) \cdot 10^{-4}$
120	$5.61 \cdot 10^{-4}$	$5.67 \cdot 10^{-4}$	$(4.63–7.13) \cdot 10^{-4}$	$(3.92–8.97) \cdot 10^{-4}$
125	$1.43 \cdot 10^{-3}$	$1.49 \cdot 10^{-3}$	$(1.22–1.87) \cdot 10^{-3}$	$(1.03–2.35) \cdot 10^{-3}$

Fermion Dark Matter, $\alpha_D = 1.0$, $M_\chi/M_{A'} = 2.0$

$M_{A'}$ (MeV)	Observed	Expected	Expected 1σ	Expected 2σ
10	$6.87 \cdot 10^{-10}$	$7.03 \cdot 10^{-10}$	$(5.71–8.91) \cdot 10^{-10}$	$(0.48–1.13) \cdot 10^{-9}$
20	$4.29 \cdot 10^{-9}$	$4.37 \cdot 10^{-9}$	$(3.58–5.49) \cdot 10^{-9}$	$(3.03–6.91) \cdot 10^{-9}$
30	$1.43 \cdot 10^{-8}$	$1.45 \cdot 10^{-8}$	$(1.18–1.82) \cdot 10^{-8}$	$(1.00–2.29) \cdot 10^{-8}$
40	$2.97 \cdot 10^{-8}$	$2.99 \cdot 10^{-8}$	$(2.44–3.76) \cdot 10^{-8}$	$(2.07–4.73) \cdot 10^{-8}$
50	$5.60 \cdot 10^{-8}$	$5.49 \cdot 10^{-8}$	$(4.48–6.92) \cdot 10^{-8}$	$(3.79–8.72) \cdot 10^{-8}$
60	$1.07 \cdot 10^{-7}$	$1.08 \cdot 10^{-7}$	$(0.88–1.35) \cdot 10^{-7}$	$(0.74–1.71) \cdot 10^{-7}$
65	$1.47 \cdot 10^{-7}$	$1.48 \cdot 10^{-7}$	$(1.21–1.87) \cdot 10^{-7}$	$(1.03–2.35) \cdot 10^{-7}$
70	$2.11 \cdot 10^{-7}$	$2.15 \cdot 10^{-7}$	$(1.76–2.71) \cdot 10^{-7}$	$(1.49–3.41) \cdot 10^{-7}$
75	$2.86 \cdot 10^{-7}$	$2.88 \cdot 10^{-7}$	$(2.36–3.63) \cdot 10^{-7}$	$(2.00–4.57) \cdot 10^{-7}$
80	$3.96 \cdot 10^{-7}$	$4.01 \cdot 10^{-7}$	$(3.27–5.04) \cdot 10^{-7}$	$(2.77–6.35) \cdot 10^{-7}$
85	$6.01 \cdot 10^{-7}$	$6.13 \cdot 10^{-7}$	$(5.01–7.71) \cdot 10^{-7}$	$(4.24–9.70) \cdot 10^{-7}$
90	$8.03 \cdot 10^{-7}$	$8.03 \cdot 10^{-7}$	$(0.66–1.01) \cdot 10^{-6}$	$(0.56–1.27) \cdot 10^{-6}$
95	$1.31 \cdot 10^{-6}$	$1.33 \cdot 10^{-6}$	$(1.09–1.67) \cdot 10^{-6}$	$(0.92–2.11) \cdot 10^{-6}$
100	$1.75 \cdot 10^{-6}$	$1.77 \cdot 10^{-6}$	$(1.45–2.23) \cdot 10^{-6}$	$(1.23–2.80) \cdot 10^{-6}$
105	$2.91 \cdot 10^{-6}$	$2.95 \cdot 10^{-6}$	$(2.41–3.70) \cdot 10^{-6}$	$(2.04–4.66) \cdot 10^{-6}$
110	$4.84 \cdot 10^{-6}$	$4.97 \cdot 10^{-6}$	$(4.06–6.25) \cdot 10^{-6}$	$(3.45–7.86) \cdot 10^{-6}$
115	$8.52 \cdot 10^{-6}$	$8.58 \cdot 10^{-6}$	$(0.70–1.08) \cdot 10^{-5}$	$(0.59–1.36) \cdot 10^{-5}$
120	$1.77 \cdot 10^{-5}$	$1.79 \cdot 10^{-5}$	$(1.46–2.25) \cdot 10^{-5}$	$(1.24–2.84) \cdot 10^{-5}$
125	$4.53 \cdot 10^{-5}$	$4.70 \cdot 10^{-5}$	$(3.84–5.91) \cdot 10^{-5}$	$(3.26–7.44) \cdot 10^{-5}$

TABLE III. The 90% CL observed limits on ε^2 for a fermion DM particle χ as a function of $M_{A'}$ for $\alpha_D = 0.1$ and $\alpha_D = 1$, and $M_\chi/M_{A'} = 2$, together with the 1 and 2 standard deviation bands around the median expected limits. The results are obtained with a data set of 7.2×10^{20} POT.

Scalar Dark Matter, $\alpha_D = 0.1$, $M_\chi/M_{A'} = 0.6$

$M_{A'}$ (MeV)	Observed	Expected	Expected 1σ	Expected 2σ
10	$2.32 \cdot 10^{-8}$	$2.36 \cdot 10^{-8}$	$(1.92–2.98) \cdot 10^{-8}$	$(1.63–3.78) \cdot 10^{-8}$
20	$5.44 \cdot 10^{-8}$	$5.56 \cdot 10^{-8}$	$(4.54–6.99) \cdot 10^{-8}$	$(3.85–8.80) \cdot 10^{-8}$
30	$1.29 \cdot 10^{-7}$	$1.31 \cdot 10^{-7}$	$(1.07–1.64) \cdot 10^{-7}$	$(0.91–2.07) \cdot 10^{-7}$
40	$2.87 \cdot 10^{-7}$	$2.91 \cdot 10^{-7}$	$(2.37–3.66) \cdot 10^{-7}$	$(2.01–4.60) \cdot 10^{-7}$
50	$5.28 \cdot 10^{-7}$	$5.39 \cdot 10^{-7}$	$(4.40–6.77) \cdot 10^{-7}$	$(3.73–8.53) \cdot 10^{-7}$
60	$9.97 \cdot 10^{-7}$	$1.01 \cdot 10^{-6}$	$(0.82–1.27) \cdot 10^{-6}$	$(0.70–1.59) \cdot 10^{-6}$
70	$1.90 \cdot 10^{-6}$	$1.90 \cdot 10^{-6}$	$(1.55–2.39) \cdot 10^{-6}$	$(1.31–3.01) \cdot 10^{-6}$
80	$2.98 \cdot 10^{-6}$	$3.02 \cdot 10^{-6}$	$(2.46–3.80) \cdot 10^{-6}$	$(2.08–4.79) \cdot 10^{-6}$
90	$5.11 \cdot 10^{-6}$	$5.11 \cdot 10^{-6}$	$(4.18–6.43) \cdot 10^{-6}$	$(3.54–8.10) \cdot 10^{-6}$
100	$7.30 \cdot 10^{-6}$	$7.33 \cdot 10^{-6}$	$(5.98–9.22) \cdot 10^{-6}$	$(0.51–1.16) \cdot 10^{-5}$
200	$1.12 \cdot 10^{-4}$	$1.15 \cdot 10^{-4}$	$(0.94–1.44) \cdot 10^{-4}$	$(0.79–1.82) \cdot 10^{-4}$
300	$2.04 \cdot 10^{-3}$	$2.08 \cdot 10^{-3}$	$(1.70–2.62) \cdot 10^{-3}$	$(1.43–3.31) \cdot 10^{-3}$
400	$9.24 \cdot 10^{-2}$	$9.19 \cdot 10^{-2}$	$(0.75–1.16) \cdot 10^{-1}$	$(0.63–1.47) \cdot 10^{-1}$

Scalar Dark Matter, $\alpha_D = 1.0$, $M_\chi/M_{A'} = 0.6$

$M_{A'}$ (MeV)	Observed	Expected	Expected 1σ	Expected 2σ
10	$7.34 \cdot 10^{-10}$	$7.46 \cdot 10^{-10}$	$(6.08–9.43) \cdot 10^{-10}$	$(0.52–1.19) \cdot 10^{-9}$
20	$1.72 \cdot 10^{-9}$	$1.76 \cdot 10^{-9}$	$(1.44–2.21) \cdot 10^{-9}$	$(1.22–2.78) \cdot 10^{-9}$
30	$4.07 \cdot 10^{-9}$	$4.14 \cdot 10^{-9}$	$(3.38–5.20) \cdot 10^{-9}$	$(2.87–6.54) \cdot 10^{-9}$
40	$9.07 \cdot 10^{-9}$	$9.20 \cdot 10^{-9}$	$(0.75–1.16) \cdot 10^{-8}$	$(0.64–1.45) \cdot 10^{-8}$
50	$1.67 \cdot 10^{-8}$	$1.70 \cdot 10^{-8}$	$(1.39–2.14) \cdot 10^{-8}$	$(1.18–2.70) \cdot 10^{-8}$
60	$3.15 \cdot 10^{-8}$	$3.18 \cdot 10^{-8}$	$(2.60–4.00) \cdot 10^{-8}$	$(2.20–5.04) \cdot 10^{-8}$
70	$6.01 \cdot 10^{-8}$	$6.00 \cdot 10^{-8}$	$(4.90–7.55) \cdot 10^{-8}$	$(4.15–9.52) \cdot 10^{-8}$
80	$9.41 \cdot 10^{-8}$	$9.55 \cdot 10^{-8}$	$(0.78–1.20) \cdot 10^{-7}$	$(0.66–1.51) \cdot 10^{-7}$
90	$1.62 \cdot 10^{-7}$	$1.61 \cdot 10^{-7}$	$(1.32–2.03) \cdot 10^{-7}$	$(1.12–2.56) \cdot 10^{-7}$
100	$2.31 \cdot 10^{-7}$	$2.32 \cdot 10^{-7}$	$(1.89–2.91) \cdot 10^{-7}$	$(1.60–3.67) \cdot 10^{-7}$
200	$3.55 \cdot 10^{-6}$	$3.63 \cdot 10^{-6}$	$(2.96–4.56) \cdot 10^{-6}$	$(2.51–5.75) \cdot 10^{-6}$
300	$6.46 \cdot 10^{-5}$	$6.58 \cdot 10^{-5}$	$(5.37–8.30) \cdot 10^{-5}$	$(0.45–1.05) \cdot 10^{-4}$
400	$2.92 \cdot 10^{-3}$	$2.91 \cdot 10^{-3}$	$(2.37–3.67) \cdot 10^{-3}$	$(2.00–4.66) \cdot 10^{-3}$

TABLE IV. The 90% CL observed limits on ε^2 for a scalar DM particle χ as a function of $M_{A'}$ for $\alpha_D = 0.1$ and $\alpha_D = 1$, and $M_\chi/M_{A'} = 0.6$, together with the 1 and 2 standard deviation bands around the median expected limits. The results are obtained with a data set of 7.2×10^{20} POT.

Fermion Dark Matter, $\alpha_D = 0.1$, $M_\chi/M_{A'} = 0.6$

$M_{A'}$ (MeV)	Observed	Expected	Expected 1σ	Expected 2σ
10	$7.36 \cdot 10^{-9}$	$6.86 \cdot 10^{-9}$	$(5.36-9.34) \cdot 10^{-9}$	$(0.44-1.32) \cdot 10^{-8}$
20	$1.58 \cdot 10^{-8}$	$1.61 \cdot 10^{-8}$	$(1.31-2.05) \cdot 10^{-8}$	$(1.10-2.64) \cdot 10^{-8}$
30	$3.45 \cdot 10^{-8}$	$3.51 \cdot 10^{-8}$	$(2.86-4.42) \cdot 10^{-8}$	$(2.42-5.59) \cdot 10^{-8}$
40	$6.64 \cdot 10^{-8}$	$6.74 \cdot 10^{-8}$	$(5.50-8.48) \cdot 10^{-8}$	$(0.46-1.07) \cdot 10^{-7}$
50	$1.17 \cdot 10^{-7}$	$1.19 \cdot 10^{-7}$	$(0.97-1.50) \cdot 10^{-7}$	$(0.82-1.89) \cdot 10^{-7}$
60	$2.17 \cdot 10^{-7}$	$2.19 \cdot 10^{-7}$	$(1.78-2.75) \cdot 10^{-7}$	$(1.51-3.46) \cdot 10^{-7}$
70	$4.12 \cdot 10^{-7}$	$4.12 \cdot 10^{-7}$	$(3.36-5.18) \cdot 10^{-7}$	$(2.84-6.53) \cdot 10^{-7}$
80	$6.61 \cdot 10^{-7}$	$6.72 \cdot 10^{-7}$	$(5.48-8.46) \cdot 10^{-7}$	$(0.46-1.07) \cdot 10^{-6}$
90	$1.18 \cdot 10^{-6}$	$1.18 \cdot 10^{-6}$	$(0.96-1.48) \cdot 10^{-6}$	$(0.81-1.87) \cdot 10^{-6}$
100	$1.81 \cdot 10^{-6}$	$1.81 \cdot 10^{-6}$	$(1.48-2.28) \cdot 10^{-6}$	$(1.25-2.87) \cdot 10^{-6}$
200	$2.30 \cdot 10^{-5}$	$2.35 \cdot 10^{-5}$	$(1.91-2.95) \cdot 10^{-5}$	$(1.62-3.73) \cdot 10^{-5}$
300	$2.75 \cdot 10^{-4}$	$2.80 \cdot 10^{-4}$	$(2.28-3.53) \cdot 10^{-4}$	$(1.93-4.46) \cdot 10^{-4}$
400	$8.13 \cdot 10^{-3}$	$8.09 \cdot 10^{-3}$	$(0.66-1.02) \cdot 10^{-2}$	$(0.56-1.30) \cdot 10^{-2}$

Fermion Dark Matter, $\alpha_D = 1.0$, $M_\chi/M_{A'} = 0.6$

$M_{A'}$ (MeV)	Observed	Expected	Expected 1σ	Expected 2σ
10	$2.33 \cdot 10^{-10}$	$2.17 \cdot 10^{-10}$	$(1.70-2.95) \cdot 10^{-10}$	$(1.40-4.16) \cdot 10^{-10}$
20	$5.01 \cdot 10^{-10}$	$5.10 \cdot 10^{-10}$	$(4.13-6.49) \cdot 10^{-10}$	$(3.49-8.33) \cdot 10^{-10}$
30	$1.09 \cdot 10^{-9}$	$1.11 \cdot 10^{-9}$	$(0.90-1.40) \cdot 10^{-9}$	$(0.77-1.77) \cdot 10^{-9}$
40	$2.10 \cdot 10^{-9}$	$2.13 \cdot 10^{-9}$	$(1.74-2.68) \cdot 10^{-9}$	$(1.47-3.38) \cdot 10^{-9}$
50	$3.69 \cdot 10^{-9}$	$3.77 \cdot 10^{-9}$	$(3.08-4.74) \cdot 10^{-9}$	$(2.61-5.97) \cdot 10^{-9}$
60	$6.86 \cdot 10^{-9}$	$6.92 \cdot 10^{-9}$	$(5.64-8.70) \cdot 10^{-9}$	$(0.48-1.09) \cdot 10^{-8}$
70	$1.30 \cdot 10^{-8}$	$1.30 \cdot 10^{-8}$	$(1.06-1.64) \cdot 10^{-8}$	$(0.90-2.06) \cdot 10^{-8}$
80	$2.09 \cdot 10^{-8}$	$2.13 \cdot 10^{-8}$	$(1.73-2.67) \cdot 10^{-8}$	$(1.47-3.37) \cdot 10^{-8}$
90	$3.72 \cdot 10^{-8}$	$3.72 \cdot 10^{-8}$	$(3.04-4.68) \cdot 10^{-8}$	$(2.58-5.90) \cdot 10^{-8}$
100	$5.71 \cdot 10^{-8}$	$5.73 \cdot 10^{-8}$	$(4.68-7.21) \cdot 10^{-8}$	$(3.96-9.08) \cdot 10^{-8}$
200	$7.26 \cdot 10^{-7}$	$7.42 \cdot 10^{-7}$	$(6.06-9.34) \cdot 10^{-7}$	$(0.51-1.18) \cdot 10^{-6}$
300	$8.69 \cdot 10^{-6}$	$8.85 \cdot 10^{-6}$	$(0.72-1.12) \cdot 10^{-5}$	$(0.61-1.41) \cdot 10^{-5}$
400	$2.57 \cdot 10^{-4}$	$2.56 \cdot 10^{-4}$	$(2.08-3.23) \cdot 10^{-4}$	$(1.76-4.10) \cdot 10^{-4}$

TABLE V. The 90% CL observed limits on ε^2 for a fermion DM particle χ as a function of $M_{A'}$ for $\alpha_D = 0.1$ and $\alpha_D = 1$, and $M_\chi/M_{A'} = 0.6$, together with the 1 and 2 standard deviation bands around the median expected limits. The results are obtained with a data set of 7.2×10^{20} POT.